Modelling of Flotation Processes by Density Functional Hydrodynamics

Oleg Yu. Dinariev, Nikolay V. Evseev*
Schlumberger Moscow Research, 13 Pudovkina str., Moscow, Russia, 119285
*nevseev@slb.com

We propose detailed microscale modelling of flotation processes by means of Density Functional Hydrodynamics (DFH), which is the direct 3D numerical modelling method for compositional flow with gas, liquid and solid phases taking into account viscosity, compressibility, interfacial tension, gravity, diffusion, and a range of rheological models. The DFH governing equations are conservation laws for chemical components, momentum and energy. The constitutive relations involve Helmholtz energy or entropy of the multicomponent multiphase mixture.

In this work, we outline the necessary background of the DFH equations. Then we demonstrate a set of relevant numerical simulations for three-phase mixtures comprising contact angles, wettability, rheological properties, and gravitational segregation. The proposed modelling is expected to help in screening and optimization in mineral processing and waste-water treatment.

1. Introduction

Flotation technology is widely used for liquid-solid separation in mineral processing and liquid-liquid separation in waste-water treatment (Russell, 2006; Fuerstenau et al., 2007; Wang et al., 2010; Wills and Finch, 2015). The typical physical mechanism in flotation is that solid particles or liquid droplets become attached to gas bubbles, and then they are transported in the mixture as aggregates due to gravitational segregation. Mathematical modelling of flotation is important for screening and optimization of this technology, including for finding opportunities for improvement in design and use of flotation machines and devices. Modern flotation theories incorporate multiscale approach involving molecular dynamics (Rai, 2012; Li et al., 2017), statistical ensembles of bubbles and particles (population balance models) (Ramkrishna, 2000; King, 2001; Marchisio and Fox, 2013), macroscopic CFD modelling of laminar and turbulent polydispersed flows using a volume fraction concept for phases in the mixture (Koh and Schwarz, 2003, 2006; Ström et al., 2013; Su et al., 2012). The detailed analysis of bubble-bubble or bubble-particle interaction provides input data for certain terms in population balance equations, and,

* nevseev@slb.com.

consequently, to the kinetic terms in macroscopic models. From our point of view, the attention paid presently to modelling of bubbles and particles systems with explicit 3D spatial and temporal resolution is insufficient. Of course, simulation of such kind cannot substitute CFD phase volume fraction modelling of industrial flotation systems, because explicit spatial resolution of small bubbles and particles for industrial installations would require prohibitively big number of computational grid cells. However, direct microfluidic modelling of polydispersed systems can improve the higher-level description that is based on distribution functions and Boltzmann-type kinetic equations (Ramkrishna, 2000; King, 2001; Marchisio and Fox, 2013). Therefore, the microfluidics is valuable in multiscale description of flotation, and this kind of microfluidic modelling is provided by the density functional hydrodynamics (DFH), which is the subject of this work.

The foundation of the DFH is the density functional theory (DFT), in which energy of a heterogeneous system is assumed to be a functional of densities of chemical components constituting the system. DFT can be traced to Thomas-Fermi model of electron gas developed in 1927; see review by Parr and Yang (1989). But the modern development of DFT was initiated by Kohn and his coauthors (Hohenberg and Kohn, 1964; Kohn and Sham, 1965). The 1998's Nobel Prize in chemistry was awarded to Walter Kohn, the major contributor in DFT development (Kohn, 1999). At present, DFT ideas are successfully applied in quantum chemistry, nuclear physics, physics of semiconductors, superconductivity, and diamagnetics.

In 1995-1998, the DFT approach was proposed in multiphase compositional hydrodynamics by Dinariev (1995, 1998), which marked the beginning of the DFH. Over the last 20 years, the DFH has been used for modelling and simulation of many practical multiphase hydrodynamic problems with account of interfacial tension, contact angles, wettability, diffusion, phase transitions (including liquid-liquid, gas-liquid, gas-solid, liquid-solid, etc.), adsorption, surfactants, rheological properties, disjoining pressure, osmosis, and gravitational segregation (Demianov et al., 2011, 2014; Ivanov et al., 2014; Armstrong et al., 2015, 2016; Dinariev and Evseev, 2016, 2017). The DFH takes advantage of the continuous description of the multiphase mixture. The primary variables are molar density of chemical components, mass velocity, and temperature. So, the DFH does not describe separate molecules; instead, it operates with physical quantities, which are smooth in respect to spatial variations. Yet the DFH description is sufficiently detailed to produce the geometry of interfaces, contact angles, and adsorption layers, which are all

modelled in both statics and dynamics. Thus, in terms of spatial resolution of the modelling, the DFH should be positioned in between molecular dynamics and population balance approaches, as illustrated schematically in Fig. 1.

The DFH governing equations involve mass, momentum, and energy conservation laws augmented with specific constitutive relations derived to ensure consistency between hydrodynamic and thermodynamic descriptions of multiphase compositional system in the frame of the density functional approach. The specific expression for the density functional uses square gradients of molar densities, which enables description of surface tension. When solid particles are present in the mixture, the dynamic equation for Almansi strain tensor is used as an additional governing equation.

In this work, we begin with exposition of the basic concepts and equations of the DFH (Section 2). The present description is a brief version of more detailed texts that can be found in our earlier publications (Demianov et al., 2014; Dinariev and Evseev, 2016, 2017). Here, we adapted DFH exposition so that it is focused on the features specific to the flotation problems.

In Section 3, we present examples of numerical simulations by DFH of various flotation problems.

In Section 4, we conclude this work by discussing the obtained results and possibilities for potential DFH applications.

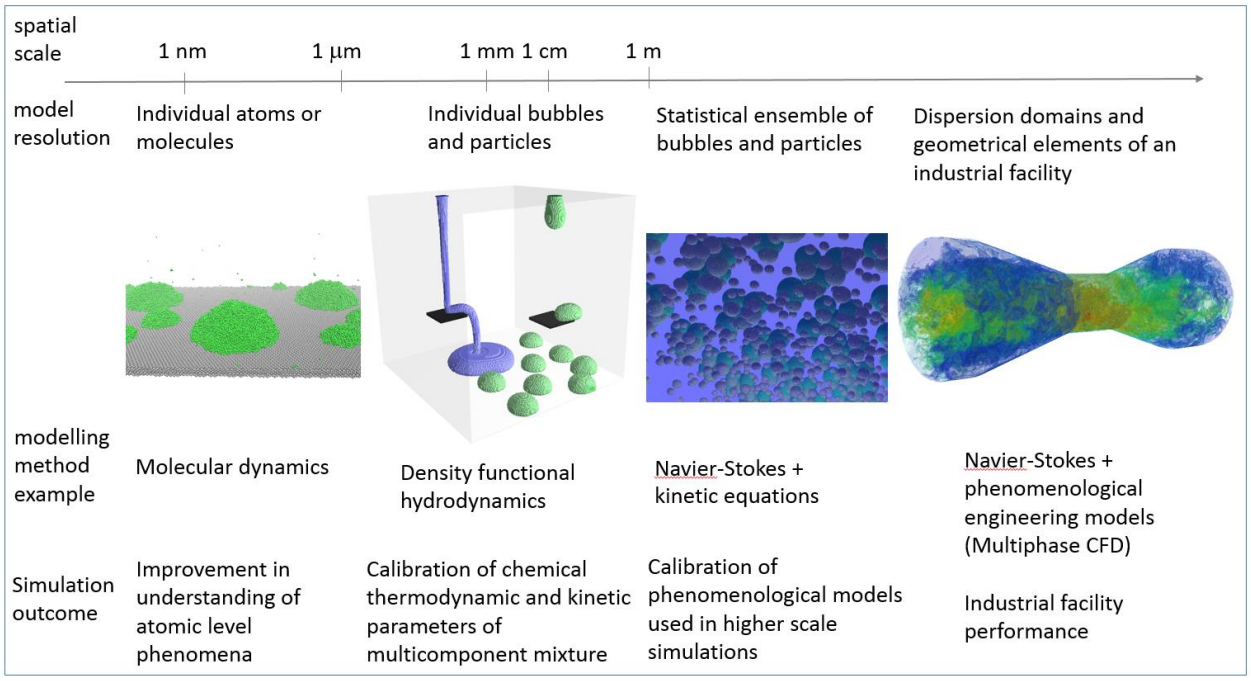


Fig.1. Schematic representation of modelling methods hierarchy at different spatial resolution and scale.

2. Basic Equations of Density Functional Hydrodynamics

We consider a multiphase mixture with M chemical components. The instantaneous state of the mixture is characterized by 3D fields of chemical component molar densities n_i, mass velocity v_a, temperature T, and Almansi strain tensor ε_{ab}. The last one is important for simulation of the mixtures with mobile solid particles, which are treated as separate phases with elastic rheology. Here and below the indices $i,j,k=1,...,M$ correspond to the chemical components, and the indices $a,b,c=1,2,3$ correspond to the Cartesian spatial coordinates. The summation over the repeated indices is implied everywhere (Einstein's rule). The following compact notations are used for the partial derivatives in respect to time t and spatial coordinates x^a: $\partial_t=\partial/\partial t$, $\partial_a=\partial/\partial x^a$.

The governing equations are hydrodynamic equations, which describe local conservation of chemical components, momentum, and energy (Sedov, 1996)

$$\partial_t n_i+\partial_a(n_i v_a+Q_{ia})=0, \tag{1}$$

$$\partial_t(\rho v_a)+\partial_b(\rho v_a v_b-p_{ab})=-n_i\partial_a\varphi_i, \tag{2}$$

$$\partial_t\varepsilon+\partial_a(\varepsilon v_a+q_a-p_{ab}v_b)=n_i\partial_t\varphi_i, \tag{3}$$

where Q_{ia} are chemical component diffusion fluxes, $\rho=m_i n_i$ is mass density, m_i are component molar masses, p_{ab} is stress tensor, φ_i are external potentials associated with chemical components in the mixture, ε is energy density, and q_a is heat flux vector. Diffusion does not transport mass, that is $m_i Q_{ia}=0$. In order to describe elastic deformations of solid particles, it is necessary to introduce dynamic equation for Almansi strain tensor ε_{ab} (Truesdell and Noll, 2004; Demianov et al., 2014)

$$\partial_t\varepsilon_{ab}=2^{-1}(\partial_b v_a+\partial_a v_b)-\varepsilon_{cb}\partial_a v_c-\varepsilon_{ac}\partial_b v_c-v_c\partial_c\varepsilon_{ab}-\tau_{\text{rel}}^{-1}\varepsilon_{ab}, \tag{4}$$

which is used together with Eqs. (1)-(3). In Eq. (4), τ_{rel} is relaxation time, which is related to viscoelastic properties of solid phase.

The system (1)-(4) is to be solved in order to obtain dynamic 3D fields of $n_i = n_i(t, x^a)$, $v_a = v_a(t, x^b)$, $T = T(t, x^a)$, and $\varepsilon_{ab} = \varepsilon_{ab}(t, x^c)$, which exhaustively describe evolution of the mixture. Yet to make the mathematical problem closed, it is necessary to specify expressions for the physical quantities other than primary variables, or, in accordance with conventional terminology, to introduce constitutive relations.

In the DFH, this is done by analysing consistency of the Eqs. (1)-(4) with well-known requirement of the non-equilibrium thermodynamics, which requires that the evolution of the system must obey the non-negative entropy production law (Prigogine, 1961). The entropy of the mixture in the spatial domain D is introduced in the following form

$$S = \int_D (s - 2^{-1} \alpha_{ij}(n_k) \partial_a n_i \partial_a n_j) dV, \tag{5}$$

where $s = s(T, n_i, \varepsilon_{ab})$ is entropy of homogeneous mixture per unit volume, and $\alpha_{ij} = \alpha_{ij}(n_k)$ is positive symmetrical matrix. The density gradient terms in Eq. (6) take account of interfacial regions, where these gradients can be significant. In isothermal problems, one uses the Helmholtz energy functional instead of entropy functional

$$F = \int_D (f + 2^{-1} \nu_{ij} \partial_a n_i \partial_a n_j + \varphi_i n_i) dV, \tag{6}$$

where $f = u - Ts$, $\nu_{ij} = T\alpha_{ij}$, and $u = u(T, n_i, \varepsilon_{ab})$ is internal energy of homogeneous mixture per unit volume.

The consistency of dynamic Eqs. (1)-(4) with entropy functional (5) or Helmholtz energy functional (6) was studied previously (Dinariev, 1995, 1998; Demianov et al., 2014; Dinariev and Evseev, 2017). We refer the reader to those publications for the help in rigorous derivation of the constitutive relations stated in below paragraphs. Here, we present the mathematical results, which are relevant for the flotation problems.

We assume that for the thermodynamic functions $s=s(T,n_i,\varepsilon_{ab})$ and $u=u(T,n_i,\varepsilon_{ab})$, one can use expressions that are commonly known in chemical thermodynamics and elasticity theory models (Walas, 1985; Demianov et al., 2014). For problems with mobile solid particles, we use elastic rheology model in accordance with the generalized Hook's law with the first and second Lamé coefficients $\lambda=\lambda(T,n_i)$ and $\mu=\mu(T,n_i)$ (Demianov et al., 2014).

Going further, we suppose that two phases are identified by molar different densities n_{i-} and n_{i+}. If one considers an equilibrium 1D solution $T=const,\ n_i=n_i(x^1),\varepsilon_{ab}=0$ describing transition from one phase n_{i-} at $x^1\to-\infty$ to another phase n_{i+} at $x^1\to+\infty$, then the interfacial tension is calculated by the following procedure (Dinariev, 1995; Demianov et al., 2014)

$$\gamma=\int_{-\infty}^{+\infty}\nu_{ij}\partial_1 n_i\,\partial_1 n_j\,dx^1. \tag{7}$$

Eq. (7) can be used to fix the parameters ν_{ij} providing that the interfacial tension γ is known from experiment.

The energy density ε is calculated in the following way

$$\varepsilon=u+\frac{1}{2}\rho v_a v_a+n_i\varphi_i, \tag{8}$$

where potentials $\varphi_i=\varphi_i(t,x^a)$ can describe various physical phenomena, such as, gravity (Dinariev, 1995), disjoining pressure and osmosis (Dinariev and Evseev, 2017), etc.

In order to write down constitutive relations for diffusion and heat fluxes, it is convenient to introduce additional notations

$$\Theta_0=T^{-1}, \tag{9}$$

$$\Theta_i=-T^{-1}\frac{\partial f}{\partial n_i}-2^{-1}\frac{\partial\alpha_{jk}}{\partial n_i}\partial_a n_j\,\partial_a n_k+\partial_a(\alpha_{ij}\partial_a n_j), \tag{10}$$

$$Q_{0a} \equiv q_a,\ \varphi_0 \equiv 0 \tag{11}$$

and assume, that indices A, B take values $0,...,M$. Then, diffusion and heat fluxes can be expressed in the following compact way

$$Q_{Aa} = \mu_{AB} \partial_a (\Theta_B - \Theta_0 \varphi_B), \tag{12}$$

with μ_{AB} being a nonnegative definite symmetric matrix with one zero eigenvalue (to provide consistency with zero mass transport by diffusion)

$$\mu_{Ai} m_i = 0. \tag{13}$$

The last step in constitutive relations is formulation of the stress tensor p_{ab}. This tensor is subdivided into static part σ_{ab}, which does not depend on velocity field v_a, and dissipative part τ_{ab}, which describe viscous phenomena,

$$p_{ab} = \sigma_{ab} + \tau_{ab}\ . \tag{14}$$

The static stress tensor is defined as follows

$$\begin{aligned}\sigma_{ab} = (f + 2^{-1} \nu_{ij} \partial_c n_i \partial_c n_j + T \Theta_i n_i) \delta_{ab} - \nu_{ij} \partial_a n_i \partial_b n_j \\ + \chi_{ab} - \chi_{ac} \varepsilon_{bc} - \chi_{bc} \varepsilon_{ac}\end{aligned}\ , \tag{15}$$

$$\chi_{ab} = \frac{\partial f}{\partial \varepsilon_{ab}}. \tag{16}$$

For the viscous stress tensor τ_{ab}, one can use the following constitutive relation

$$\tau_{ab} = \eta_v \delta_{ab} \partial_c v_c + \eta_s (\partial_a v_b + \partial_b v_a - \frac{2}{3} \delta_{ab} \partial_c v_c) \tag{17}$$

with η_{v} and η_{s} being nonnegative bulk and shear viscosity coefficients, respectively. In linear viscous model, these coefficients can depend on local temperature and component densities. In nonlinear viscous models, they can depend also on local velocity gradients.

As a conclusion to this section, we put here a brief summary on how various multiphase phenomena are accounted for in the frame of the DFH.

- Interfacial tension is taken into account by the means of the molar density gradient term that enters the expression for entropy (5) or Helmholtz energy (6). Assuming γ is known from experiment Eq. (7) is solved numerically to find parameters ν_{ij}.
- Adsorption (e.g., surfactants) into interfacial area between mobile liquid phases is incorporated into the theory by the dependence of coefficients α_{ij} in Eq. (6) on local composition.
- Wettability (interfacial tension between liquid and solid) and adsorption onto solid boundaries are described by the boundary condition in Eq. (21).
- Coalescence and breakup of droplets and bubbles, as well as any other topological changes of interfacial boundaries, happen naturally and can be traced from evolution of molar density fields.
- DFH is not limited to Newtonian rheology and can handle non-Newtonian rheologies by using appropriate expression for viscous stress tensor. In particular, visco-elastic, visco-elasto-plastic, as well as the well-known Herschel-Bulkley rheological models can be employed by using appropriate expressions for τ_{ab}.
- Phase transitions are governed by the bulk entropy or Helmholtz energy properties following the principles of chemical thermodynamics.
- Hydrodynamic Eqs. (1)-(4) are solved in each spatial point of a domain containing multicomponent mixture. Accordingly, the evolution of the system is described by the evolution of molar densities of chemical components and mass velocity. For multiphase mixtures, the position of an interface is indicated by high molar density gradients.
- Equilibrium multiphase states without motion satisfy conditions that $v_a = 0$ and quantities $\Theta_A - \Theta_0 \varphi_A$, used in Eq. (12), are constant in both time and space.

- There are extensions of DFH published elsewhere (Demianov et al., 2014; Dinariev and Evseev, 2017) that significantly widen the range of phenomena that can be modeled.

As explained in our previous publications (Demianov et al., 2014; Dinariev and Evseev, 2017), the boundary conditions for the governing Eqs. (1)-(4), depending on a particular problem, can include slip or no-slip conditions for mass velocity, wetting conditions at solid walls, and source and sink conditions.

3. Numerical simulation examples

Floatability of suspended matter (solid particles or liquid droplets) depends on the number of factors and have been extensively discussed in the literature (Nguyen and Schulze, 2003; Fuerstenau et al., 2007; Wang et al., 2010). In general case, the major factors influencing the chances for the floating up bubble to capture a suspended particle (or droplet) can be split in the following two groups:

(1) Interfacial energy balance. Capture is possible if there is a reduction in combined interfacial energy of both bubble and particle due to their contact after capture; such reduction occurs in case of hydrophobic, or aerophilic suspended matter.

(2) Hydrodynamic conditions of a collision. While for slow moving bubbles and particles the capturing probability depends almost exclusively on the interfacial energy balance, in faster moving conditions, velocity and trajectory of a bubble relative to a particle become important (Dai et al., 1998; Ralston et al., 1999).

The detailed study of the factors in the first group was a subject of numerous publications. The comprehensive explanation of the associated phenomena involves nanoscale description of the electromagnetic interactions between the molecules, van der Waals forces, and disjoining pressure (Derjaguin, 1989; Bonn et al., 2009; Pan et al., 2011). The interfacial phenomena associated with disjoining pressure can also be modelled numerically in the frame of the DFH (Dinariev and Evseev, 2017).

However, in practical problems of flotation, dimensions of the domains of interest such as bubbles, droplets, and particles are microscale or even millimeter-scale. Therefore, conducting direct numerical simulation of those domains while maintaining nanoscale modelling resolution is not feasible. Yet, using the DFH, the necessary interfacial phenomena can be effectively and

properly captured at coarser resolution models (Demianov et al., 2011, 2014; Armstrong et al., 2015, 2016; Dinariev and Evseev, 2016). According to the theory described in Section 2, DFH enables direct simultaneous modelling of both interfacial and inertial phenomena important for consistent description of flotation mechanisms throughout wide range of flow regimes.

In this section, we present numerical simulation of several problems relevant for flotation processes. In each case, the numerical simulations have been performed by solving the DFH Eqs. (1)-(4) together with the constitutive relations in Eq. (9)-(17). We followed our standard simulation workflow; here we describe only the details directly related to the problems solved while omitting the details of more general nature, which an inquisitive reader can find in our earlier publications such as (Demianov et al., 2014; Armstrong et al., 2016; Dinariev and Evseev, 2016, 2017).

3.1. Example 1. Collisions at different hydrodynamic regimes

We begin by presenting simulation examples involving a single droplet or particle and a single bubble. We pursue demonstration at different hydrodynamic regimes, and in order to have that we vary reference size of the suspended matter and air bubbles. The problem statements used here provide necessary convenience for detailed study of the basic capture mechanisms.

A three-component mixture was used in the modelling. To describe thermodynamic behaviour of the mixture, a polynomial approximation of the Helmholtz free energy near three equilibrium phases, Phases A, B, and C, was employed (Armstrong et al., 2016; Dinariev and Evseev, 2017); Phase A is always liquid, Phase B can be liquid or solid, and Phase B is always gaseous. The phases were defined in such a way that each of the Phases A, B, and C constituted 100% of components 1,2, and 3, respectively. The relevant properties of phases and components were as follows: $\rho_{\mathrm{A}} = 1000$ kg/m^3, $\rho_{\mathrm{B}} = 1000$ kg/m^3, $\rho_{\mathrm{C}} = 1.4$ kg/m^3, $\eta_{\mathrm{sA}} = 0.001$ Pa · s, $\eta_{\mathrm{sB}} = 0.01$ Pa · s, $\eta_{\mathrm{sC}} = 2 \cdot 10^{-5}$ Pa · s, $\gamma_{\mathrm{AB}} = 0.017$ N/m, $\gamma_{\mathrm{BC}} = 0.035$ N/m, $\gamma_{\mathrm{CA}} = 0.024$ N/m; here, $\rho_{\mathrm{A}}, \rho_{\mathrm{B}}, \rho_{\mathrm{C}}$ and $\eta_{\mathrm{sA}}, \eta_{\mathrm{sB}}, \eta_{\mathrm{sC}}$ are mass densities and shear viscosities of Phases A, B, and C, respectively, and $\gamma_{\mathrm{AB},}\, \gamma_{\mathrm{CA}}, \gamma_{\mathrm{BC}}$ are the interfacial tensions between the three pairs of phases A-B, C-A, and B-C, correspondingly.

The contact angles on the triple contact line (Fig. 3.1) are related by the following equation (Rowlinson and Widom, 1982)

$$\frac{\sin\alpha_{\mathrm{A}}}{\gamma_{\mathrm{BC}}}=\frac{\sin\alpha_{\mathrm{B}}}{\gamma_{\mathrm{CA}}}=\frac{\sin\alpha_{\mathrm{C}}}{\gamma_{\mathrm{AB}}}, \tag{3.1}$$

where $\alpha_{\mathrm{A}},\alpha_{\mathrm{B}},\alpha_{\mathrm{C}}$ are the contact angles bound by the condition $\alpha_{\mathrm{A}}+\alpha_{\mathrm{B}}+\alpha_{\mathrm{C}}=360^{\circ}$. Three phase contact breaks when one of the interfacial tensions becomes greater than the sum of two others. In that case, a layered contact develops, in which one of the phases forms a continuous layer between the pair of phases having maximum interfacial tension among all of the three pairs. A layer of oil on an oil contaminated water surface, or an air film over a strongly hydrophobic particle suspended in water, are two examples of such situation. For the interfacial tensions specified above, the corresponding contact angles calculated using Eq. (3.1) are $\alpha_{\mathrm{A}}=80^{\circ}$, $\alpha_{\mathrm{B}}=132^{\circ}$, and $\alpha_{\mathrm{C}}=148^{\circ}$. These angles mean that a particle or droplet made of Phase B is hydrophobic given that Phase A is water.

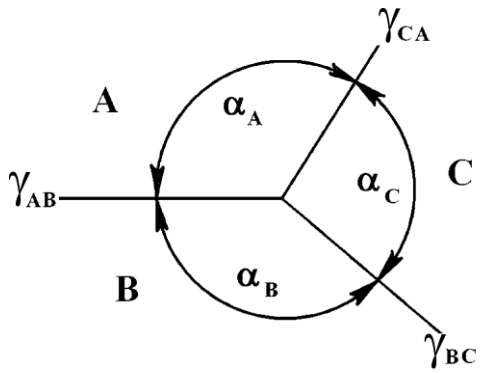


Fig. 3.1. Schematic representation of a triple contact line

Two series of simulations with two cases within each series have been carried out on a vertical parallelepiped model with dimensions 1.8 mm × 1.8 mm × 4.5 mm in Case 1 and 9 mm × 9 mm × 22.5 mm in Case 2. In each case the model was approximated by 120 × 120 × 250 cubic cells. The model was periodic in both of the lateral dimensions, that is periodic boundary conditions have been established on the lateral sides of the model. The top and bottom sides of the model were impermeable walls. The gravity field with gravitational acceleration equal to $g_z=10$ m/s^2 was acting downwards in vertical direction.

The initial conditions for the modelling (Fig. 3.2) were as follows. The model was filled with water (Phase A) and a gas bubble of Phase C was placed within the model near its bottom and shifted slightly left from the vertical axis of symmetry of the model. Also, a liquid droplet of Phase B was suspended in the middle of the model (Fig. 3.2a). In Series 2, a suspended solid particle was placed instead of the droplet (Fig. 3b). In case of the solid particle, viscosity of Phase B is irrelevant; instead, the Lamé coefficients were assigned to Phase B, $\lambda_{\mathrm{B}} = \mu_{\mathrm{B}} = 10^6$ Pa (as we have explained in (Demianov et al., 2014, pp. 247-248), due to relatively small stresses present in moving liquid in typical scenarios, all Lamé coefficients on the order of $\sim 10^6$ and higher are equal in a sense that the shape of solid particles is well maintained).

In accordance with the model dimensions, the diameter of the bubble, $2r_{\mathrm{b}}$, was 0.51 mm in Case 1 and 2.55 mm in Case 2, and the diameter of the droplet was 0.9 mm in Case 1 and 4.5 mm in Case 2. The solid particle used in Series 2 was axisymmetric along the longitudinal axis, which had length equal to 1.14 mm in Case 1 and 5.7 mm in Case 2.

Due to the difference in dimensions, the two cases in each series are distinct in hydrodynamic regime. In Case 1, the bubble is relatively slow-moving, while in Case 2 it is rather fast moving. Indeed, according to the Hadamard-Rybczynski formula (Levich, 1962), the terminal velocity of a rising bubble is

$$v_{\mathrm{HR}} = \frac{2(\rho_{\mathrm{B}} - \rho_{\mathrm{A}}) g_z r_{\mathrm{b}}^2}{3\eta_{\mathrm{sA}}} \frac{\eta_{\mathrm{sA}} + \eta_{\mathrm{sB}}}{2\eta_{\mathrm{sA}} + 3\eta_{\mathrm{sB}}}, \tag{3.2}$$

which gives 21 cm/s in Case 1 and 5.3 m/s in Case 2 (with the reservation that in Case 2, an exaggerated value is produced by the Hadamard-Rybczynski Eq. (3.2) since its only valid for spherical bubbles and low Reynolds numbers, Re < 1). The actual velocities observed in the simulations are only a portion of that predicted by Eq. (3.2), because of the model size and collective effects.

The simulation results for Case 1 of Series 1 are shown in Fig. 3.3 in a form of consecutive movie frames captured at separate moments in time 0.03 s, 0.034 s, 0.045 s, 0.051 s, and 0.106 s. To facilitate observation of contact phenomena, the bottom row of the images in Fig. 3.3 show the model in cross-section at the same moments in time.

The first pair of images (top and bottom) corresponding to 0.03 s is captured at the moment when the bubble just starts being influenced by the presence of the suspended droplet (the droplet does not move yet, since to facilitate the detailed observation of all stages of the contact phenomena, its mass density has been selected to be exactly the same as that of the ambient liquid). At the next pair of images at 0.034 s, slight deformation of surfaces of both the bubble and the droplet becomes visible. The deformation indicates elastic response of the interfaces to inertial collision. Then, at 0.045 s, only a water film separates the bubble and the droplet while the energy of the collision has been dissipated by viscous friction and the interfaces retained their round shape. At 0.051 s, the full contact has established; a close inspection of the cross-section shows correct angles. Finally, at the end of the simulation, due to buoyancy, the bubble came at the top of the droplet and the whole agglomerate begins rising at a slow pace.

In Case 2 of Series 1 (Fig. 3.4), the movie frames correspond to moments in time 0.047 s, 0.055 s, 0.065 s, 0.08 s, and 0.121 s. Here the bubble is big and its rising velocity is high enough to cause noticeable change in shape from spherical to ellipsoidal – the transition that occurs with Reynolds number approaching ~30 (Clift et al., 1978). The images taken at 0.055 and 0.065 s show considerable deformation of interfaces owing to much bigger inertial phenomena than in previous Case 1. Although the bubble and droplet collide as is visible at 0.08 s, they do not stay in contact; complete detachment occurs at 0.121 s. This the manifestation of importance of accounting for both interfacial and inertial phenomena in modelling of the general case flotation mechanisms.

The simulation results are qualitatively similar for the simulation Series 2 where the suspended solid particle was used instead of the liquid droplet. Fig. 3.5 shows the results for Case 1 and Fig.3.6 for Case 2.

The consecutive movie frames for Case 1 of Series 2 were captured at 0.034 s, 0.041 s, 0.047 s, 0.076 s, and 0.126 s. The rising bubble undergoes only very slight deformation in getting close to the suspended particle. After the water is pushed from between the bubble and the particle, a firm contact is established. The particle is captured and is floated up to the top of the model.

In Case 2 of Series 2, the consecutive movie frames have been captured at 0.048 s, 0.057 s, 0.075 s, 0.093 s, and 0.126 s. Similarly to the corresponding case of Series 1, the bubble rises in ellipsoidal shape regime, and there is a huge deformation of the bubble at 0.057 s when it collides with the particle (there is no deformation of the solid particle, of course, because the particle was modelled using the elastic rheology model). Although there is a firm contact between the bubble

and the particle while the bubble still stays below the particle, the bubble drops the particle once it finally moves above the latter.

Thus, in this subsection, we demonstrated direct numerical simulation of the bubble-droplet and bubble-particle capture mechanisms in different inertial regimes. Previously, those mechanisms have been extensively studied by using approximate analytical and semi-analytical models (Dai et al., 1998; Ralston et al., 1999).

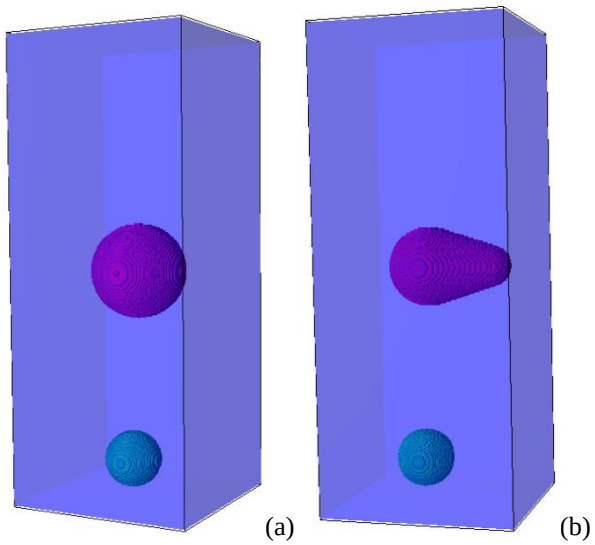
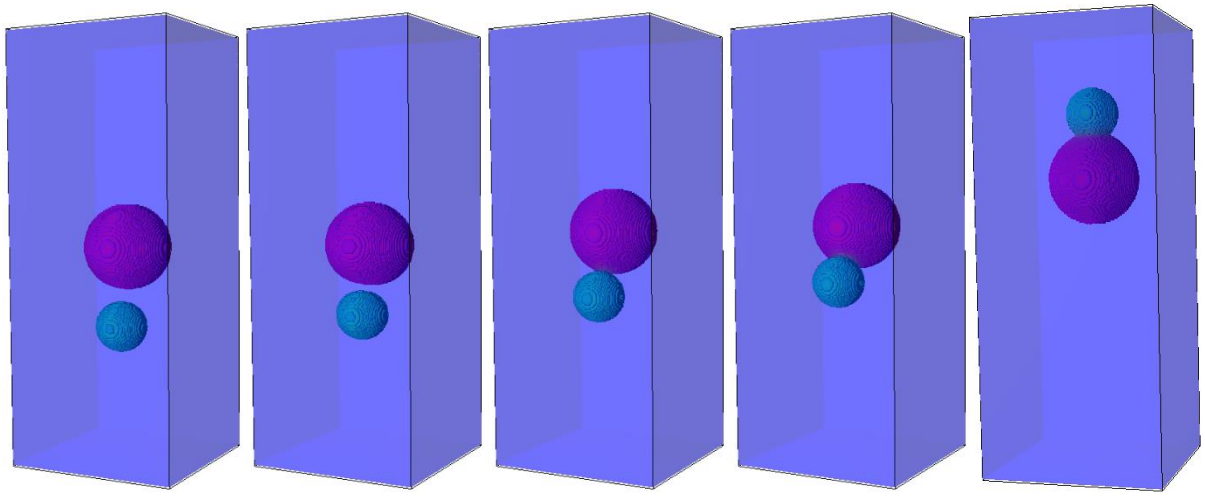


Fig. 3.2. Example 1. 3D view of the initial conditions for simulating Series 1 (a) and Series 2 (b). The ambient liquid of Phase A is shown in semitransparent blue, the gas bubble of Phase C is shown in green, and the suspended matter of Phase B is shown in red.



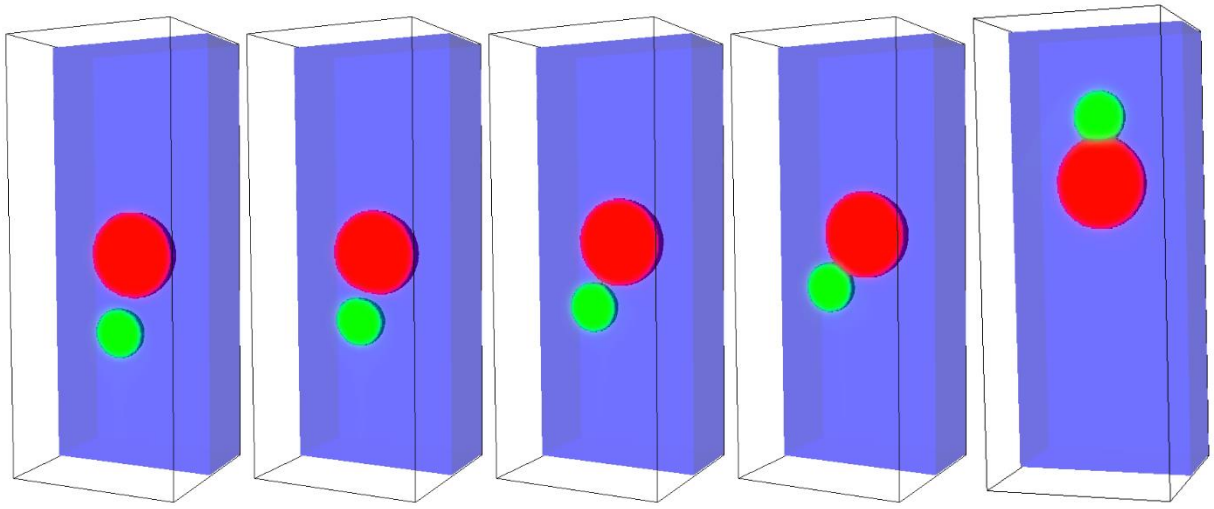
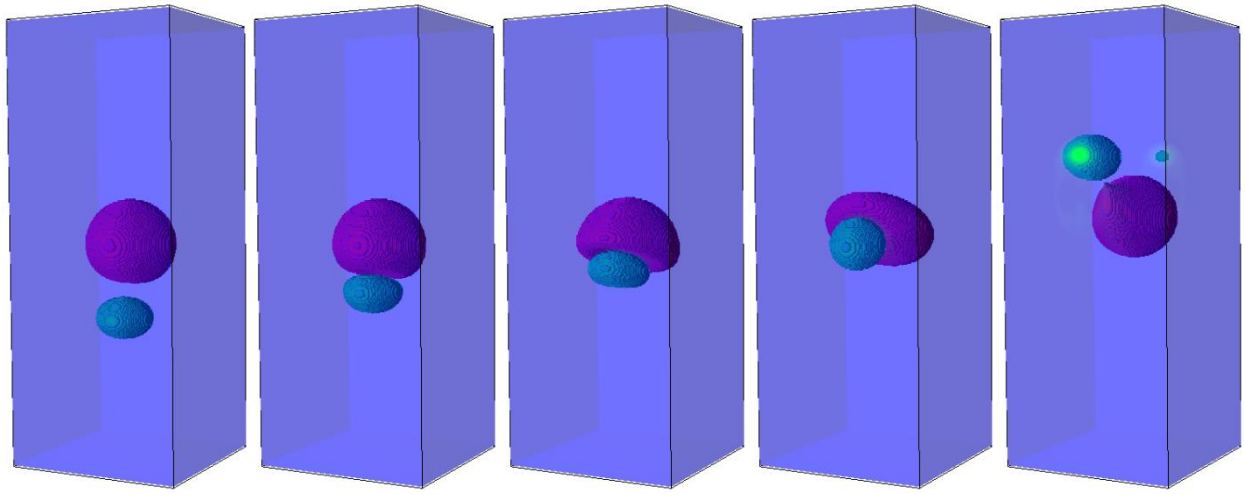


Fig. 3.3. Example 1, Series 1, Case 1. 3D view of the model at consecutive moments in time (top row), and the same in cross-section (bottom row). The ambient liquid of Phase A is shown in semitransparent blue, the gas bubble of Phase C is shown in green, and the liquid droplet of Phase B is shown in red.



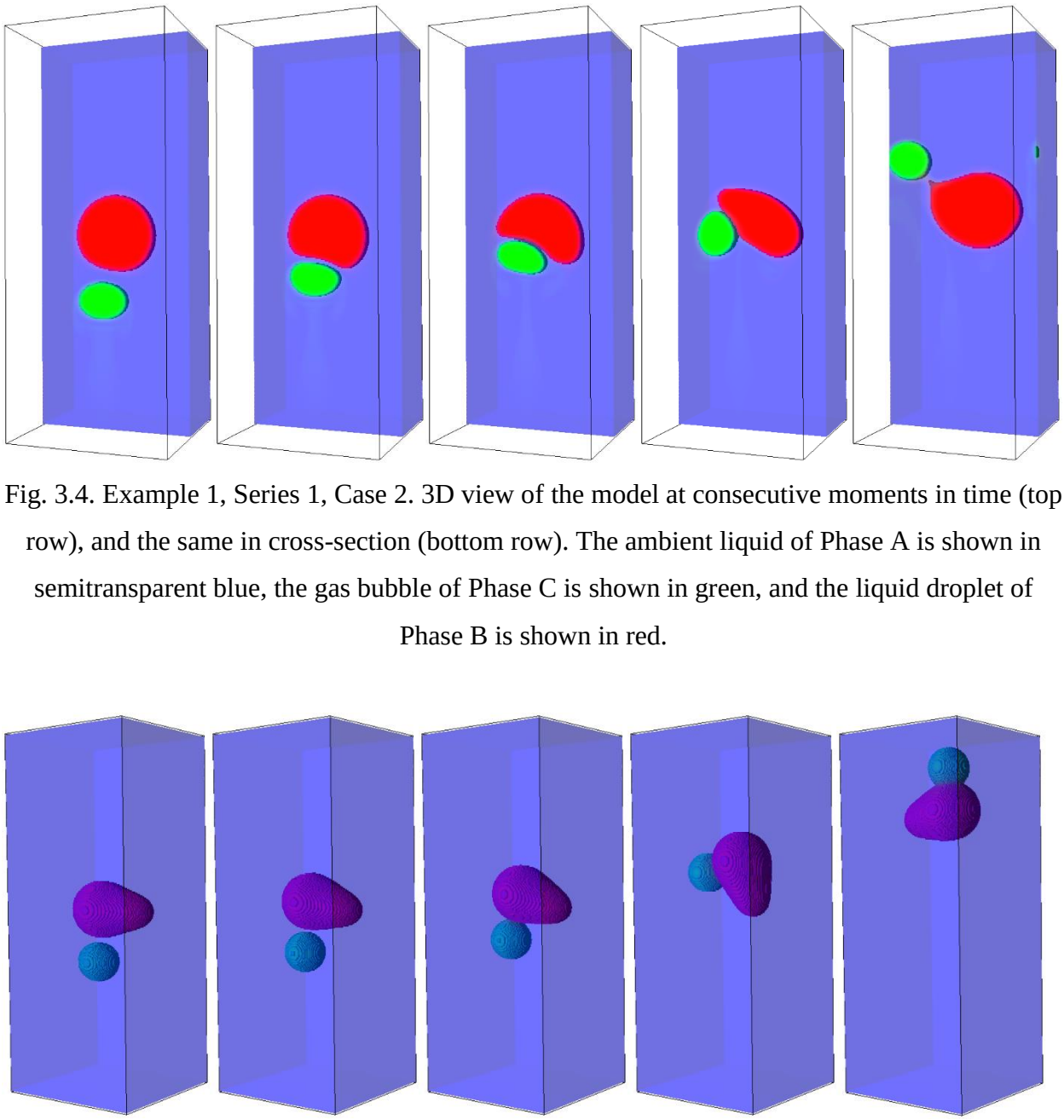


Fig. 3.4. Example 1, Series 1, Case 2. 3D view of the model at consecutive moments in time (top row), and the same in cross-section (bottom row). The ambient liquid of Phase A is shown in semitransparent blue, the gas bubble of Phase C is shown in green, and the liquid droplet of Phase B is shown in red.

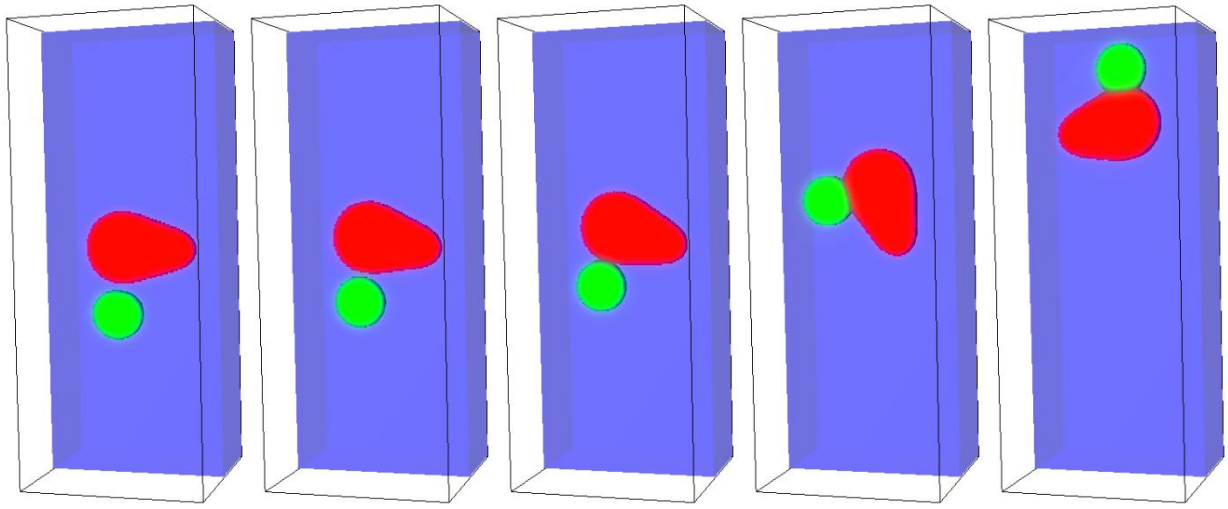
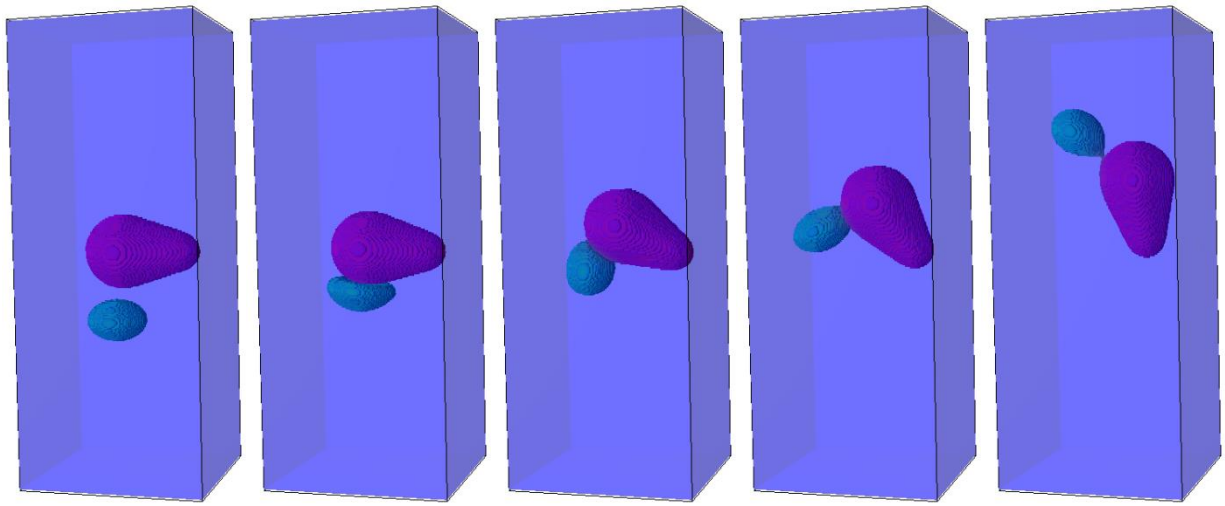


Fig. 3.5. Example 1, Series 2, Case 1. 3D view of the model at consecutive moments in time (top row), and the same in cross-section (bottom row). The ambient liquid of Phase A is shown in semitransparent blue, the gas bubble of Phase C is shown in green, and the solid particle of Phase B is shown in red.



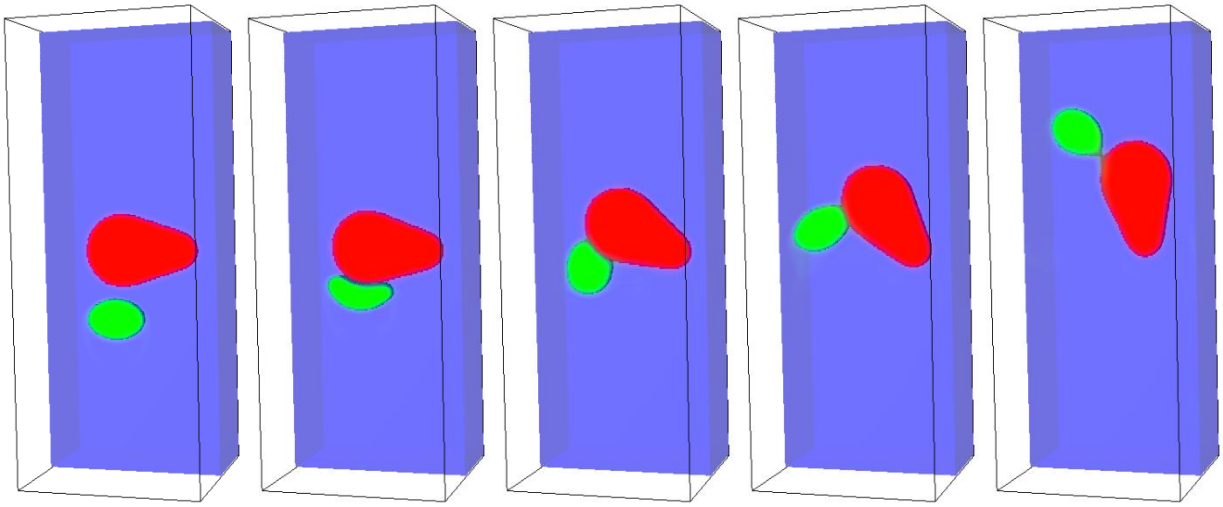


Fig. 3.6. Example 1, Series 2, Case 2. 3D view of the model at consecutive moments in time (top row), and the same in cross-section (bottom row). The ambient liquid of Phase A is shown in semitransparent blue, the gas bubble of Phase C is shown in green, and the solid particle of Phase B is shown in red.

3.2. Example 2. Hydrophobic and hydrophilic suspended matter

In this subsection, we demonstrate more complex statements involving many bubbles and suspended liquid droplets or solid particles. We also vary interfacial tensions to obtain statements with hydrophobic or hydrophilic suspended matter.

Two simulation series have been carried out. In Series 1, the suspended matter was liquid droplets, while in Series 2 it was solid particles. The model used in the simulations of Series 2 was a vertical parallelepiped model with dimensions 0.6 mm × 0.6 mm × 0.9 mm approximated by 200 × 200 × 300 cubic cells. In Series 2, the parallelepiped was slightly smaller with dimensions 0.45 mm × 0.45 mm × 0.675 mm approximated by 150 × 150 × 225 cubic cells.

The models were periodic in both of the lateral dimensions. The top and bottom sides of the models were impermeable walls. The gravity field was acting downwards in vertical direction.

The properties of phases and components were the same as those of the Subsection 3.1, except for the interfacial tensions that were varied here. Within each of the series, three cases different in interfacial tension (Table 1) have been used for numerical simulation. All other conditions across the cases were the same.

Table 1. The scope of interfacial tensions between three pairs of phases and corresponding contact angle α_A

	γ_{AB}, N/m	γ_{BC}, N/m	γ_{AC}, N/m	$\gamma_{BC}/(\gamma_{AB}+\gamma_{AC})$	α_A, °
Case 1	0.03	0.025	0.025	0.45	80
Case 2	0.017	0.035	0.024	0.85	127
Case 3	0.015	0.05	0.02	1.42	–

Fig. 3.2.1 shows initial conditions for the simulations. In cases of Series 1, three liquid droplets of Phase B (shown in red) have been suspended within the liquid of Phase A (shown in semitransparent blue). The droplets are spherical with slightly unequal diameters near 200 μm. Below the droplets, 30 bubbles with diameters in between 33 μm and 54 μm were scattered. In cases of Series 2, two solid particles of slightly different shape have been suspended near the bottom of the model. Both particles are symmetric along the longitudinal axis, which has length of 225 μm for the bigger particle and 175 μm for the smaller one. Around the particles, 17 bubbles with diameter range like in Series 1 were scattered.

The numerical simulation results for the three cases of Series 1 are presented in Figs. 3.2.2 through 3.2.5 in a form of separate movies frames. In Case 1 (Fig. 3.2.2), four successive frames labeled as (a) through (d) correspond to consecutive moments in time 0.24 s, 0.525 s, 0.723 s, and 1.05 s. Figs. 3.2.3 and 3.2.4 demonstrate similarly arranges frames for the Cases 2 and 3, respectively, but the time moments there are different: 0.24 s, 0.603 s, 0.996 s, and 1.488 s for Fig. 3.2.3, and 0.24 s, 0.546 s, 0.855 s, and 1.5 s for Fig. 3.2.4. Finally, Fig. 3.2.5 shows in 3D cross-section one individual selected movie frame for each of the cases. Those cross-sections are suitable for observation of contact angles.

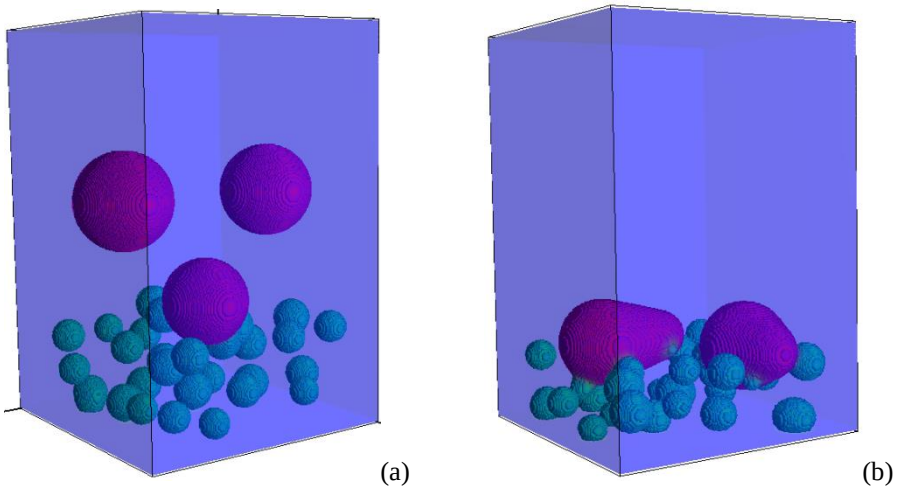
In Case 1, most of the floating up bubbles immediately attach to the suspended droplets since the interfacial tension between the droplets and the bubbles is smaller than between the droplets and the surrounding liquid (Table 1). Only the bubbles that passed without touching the droplets missed in this case. The droplets are quickly drawn upwards and in 1.5 s all of them have reached the top of the model. In this case, the droplets can be described as hydrophobic, or aerophilic.

In Case 2 (Fig. 3.2.3), the interfacial tension between the gas and the liquid droplets is higher than in Case 1, but it is still not yet high enough to cause the inequality $\gamma_{BC} > \gamma_{AB} + \gamma_{AC}$ to

become fulfilled (Table 1). Fulfilling this inequality would mean that direct contact between Phases B and C, that is between gas and liquid droplets, is not possible at all. But here, the contact is still possible, though the contact angle α_A is significantly smaller than in Case 1. Therefore, the chance for the bubbles to "miss" droplets becomes considerably bigger. By looking at the frames in Fig. 3.2.3, one can observe that many bubbles have indeed missed. Much fewer ones have attached to the droplets to pull them up. Eventually, the droplets have floated to the top of the model, but the process took more time than in Case 1.

Finally, in Case 3 the condition $\gamma_{BC} > \gamma_{AB} + \gamma_{AC}$ holds. Therefore, direct contact between Phases B and C, that is between gas and liquid droplets, is not possible. Such liquid droplets are completely hydrophilic, or aerophobic. As a result, not a single bubble is captured, and the droplets settle down (Fig. 3.2.4).

The results for Series 2 are shown in Figs. 3.2.6 through 3.2.9. Similarly to Series 1 presentation, the figures show consecutive movie frames captured at different moments in time for Case 1 (Fig. 3.2.6), Case 2 (Fig. 3.2.7), and Case 3 (Fig.3.2.8). Fig. 3.2.9 is used to present the results in cross-sections (the apparent change in shape of the particle is resulting from different particle orientation in images (a) and (b) caused by interactions with bubbles). Since interfacial tensions used in both series are the same, most of the comments made for Series 1 are valid for Series 2 as well. The only fundamental difference between the series is in the solid nature of Phase B, which reduces its mobility in ambient liquid compared to the case when Phase B is also a liquid. However, exact evaluation of this effect should be the subject of a separate specifically focused study; the present simulations are aimed at demonstration of the possibilities of the modelling.



(a) (b)

Fig. 3.2.1. Example 2. 3D view of the initial conditions for simulating Series 1 (a) and Series 2 (b). The ambient liquid of Phase A is shown in semitransparent blue, the gas bubbles of Phase C are shown in green, and the suspended matter of Phase B is shown in red.

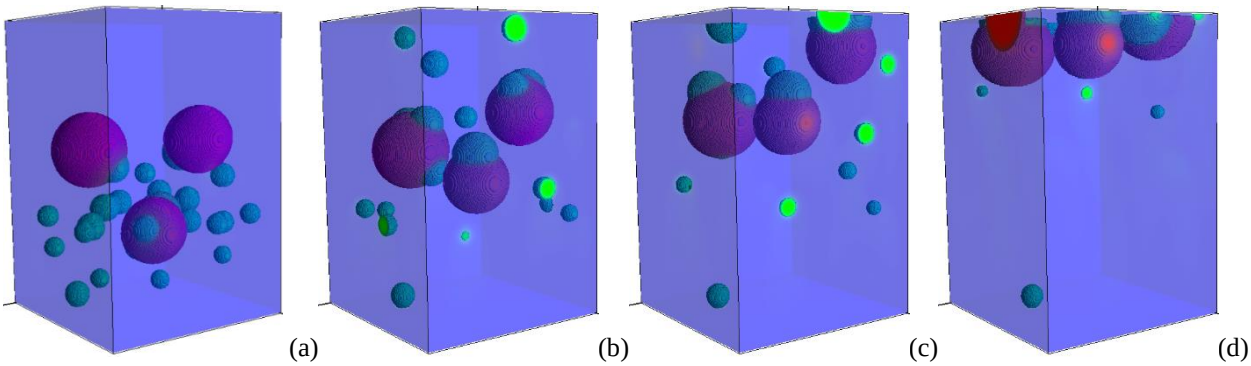


Fig. 3.2.2. Example 2, Series 1, Case 1. 3D view of the bubbles and droplets distributions at consecutive moments in time 0.24 s (a), 0.525 s (b), 0.723 s (c), and 1.05 s (d). The ambient liquid of Phase A is shown in semitransparent blue, the gas bubbles of Phase C are shown in green, and the liquid droplets of Phase B are shown in red.

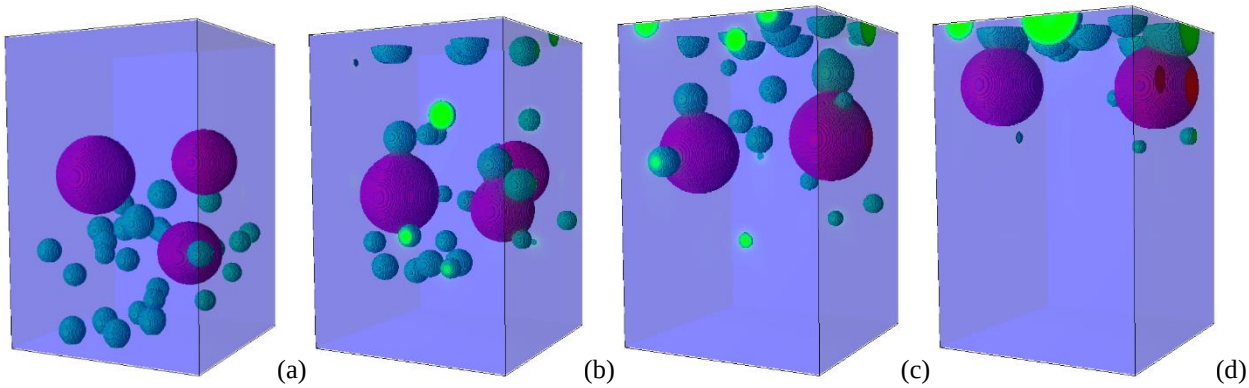


Fig. 3.2.3. Example 2, Series 1, Case 2. 3D view of the bubbles and droplets distributions at consecutive moments in time 0.24 s (a), 0.603 s (b), 0.996 s (c), and 1.488 s (d). The ambient liquid of Phase A is shown in semitransparent blue, the gas bubbles of Phase C are shown in green, and the liquid droplets of Phase B are shown in red.

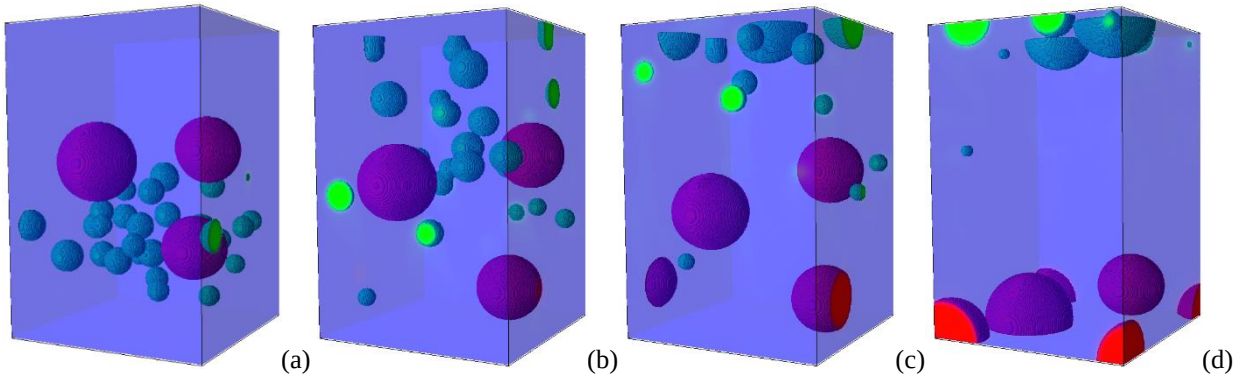


Fig. 3.2.4. Example 2, Series 1, Case 3. 3D view of the bubbles and droplets distributions at consecutive moments in time 0.24 s (a), 0.546 s (b), 0.855 s (c), and 1.5 s (d). The ambient liquid of Phase A is shown in semitransparent blue, the gas bubbles of Phase C are shown in green, and the liquid droplets of Phase B are shown in red.

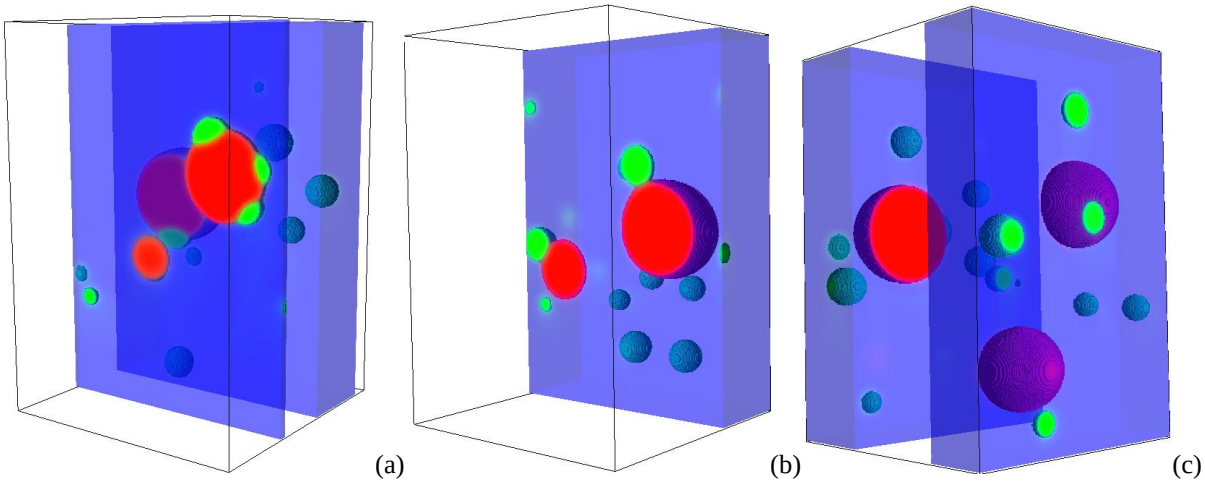


Fig. 3.2.5. Example 2. Selected examples of 3D views in cross-sections for the distribution of bubbles and droplets in Series 1; Case 1 (a), Case 2 (b), and Case 3 (c). The ambient liquid of Phase A is shown in semitransparent blue, the gas bubbles of Phase C are shown in green, and the liquid droplets of Phase B are shown in red.

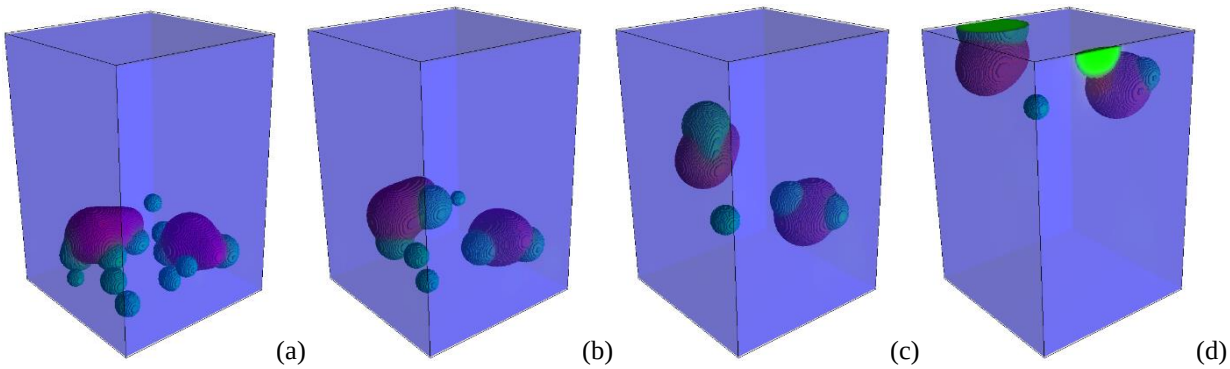


Fig. 3.2.6. Example 2, Series 2, Case 1. 3D view of the bubbles and solid particles distributions at consecutive moments in time 0.06 s (a), 0.237 s (b), 0.483 s (c), and 0.951s (d). The ambient liquid of Phase A is shown in semitransparent blue, the gas bubbles of Phase C are shown in green, and the solid particles of Phase B are shown in red.

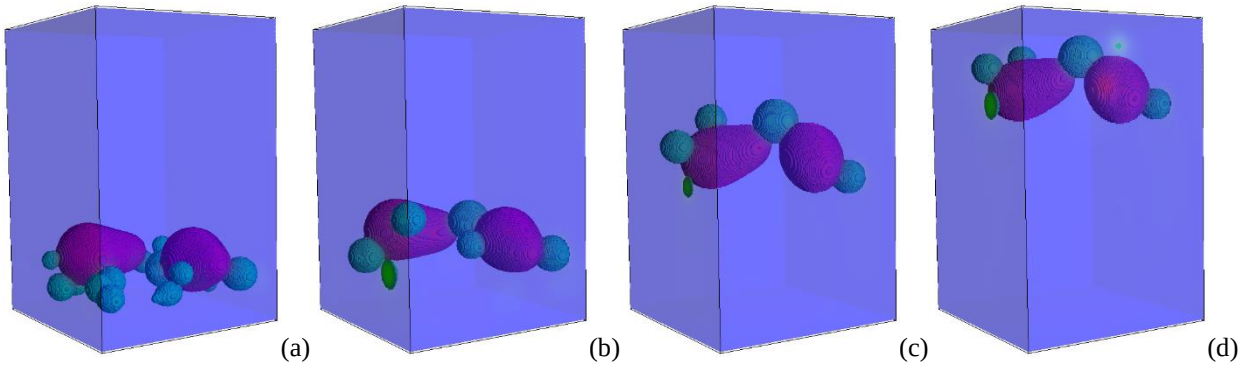


Fig. 3.2.7. Example 2, Series 2, Case 2. 3D view of the bubbles and solid particles distributions at consecutive moments in time 0.06 s (a), 0.309 s (b), 0.63 s (c), and 0.861s (d). The ambient liquid of Phase A is shown in semitransparent blue, the gas bubbles of Phase C are shown in green, and the solid particles of Phase B are shown in red.

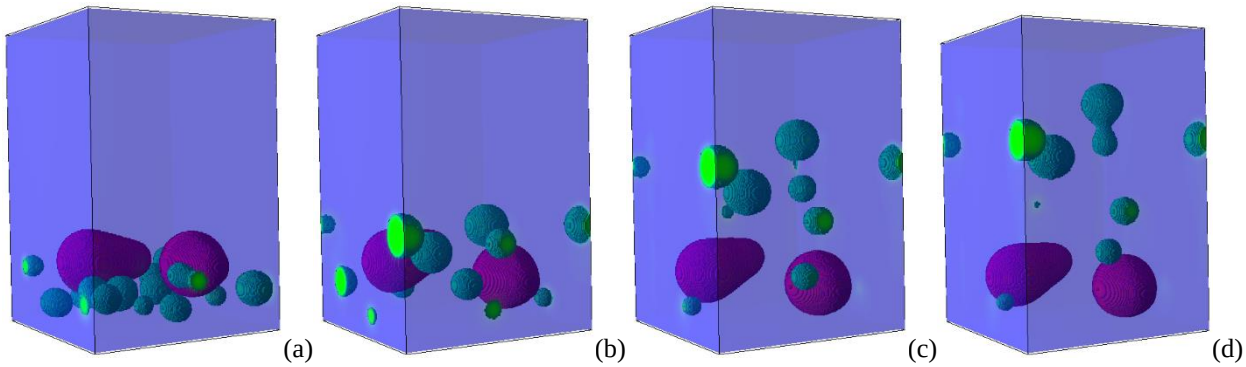


Fig. 3.2.8. Example 2, Series 2, Case 3. 3D view of the bubbles and solid particles distributions at consecutive moments in time 0.06 s (a), 0.234 s (b), 0.272 s (c), and 0.432 s (d). The ambient liquid of Phase A is shown in semitransparent blue, the gas bubbles of Phase C are shown in green, and the solid particles of Phase B are shown in red.

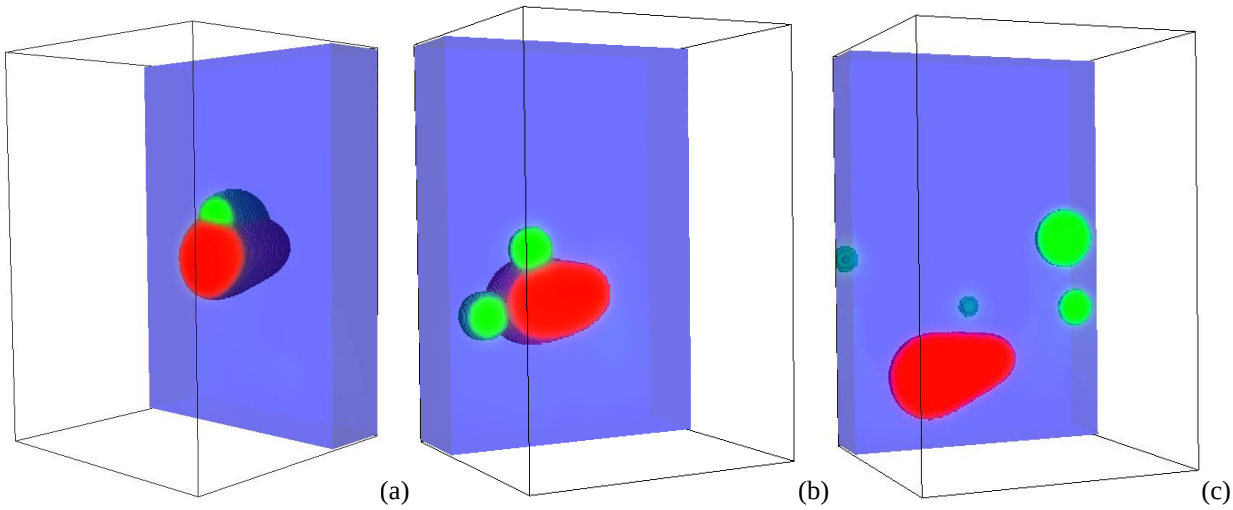


Fig. 3.2.9. Example 2. Selected examples of 3D views in cross-sections for the distribution of bubbles and solid particles in Series 2; Case 1 (a), Case 2 (b), and Case 3 (c). The ambient liquid of Phase A is shown in semitransparent blue, the gas bubbles of Phase C are shown in green, and the solid particles of Phase B are shown in red.

3.3. Example 3. Dissolved air flotation

For simulation of the dissolved air flotation (DAF) it is necessary to model phase transitions phenomena, which is explicitly captured by DFH as was demonstrated in our previous publications (Demianov et al., 2011, 2014; Dinariev and Evseev, 2016).

The difference between problem statement used here and in the previous Subsection 3.2 is in initial conditions. Here, we do not put any bubbles in the initial conditions; instead, we uniformly dissolve the gas within the ambient liquid (Fig. 3.3.1). As per definition of the thermodynamic model we used in this modelling, the phases have been defined as pure that is any mixing of phases forms thermodynamically unstable solution (see the mixture description in Subsection 3.1). The interfacial tensions correspond to Case 1 of Subsection 3.1.

Two cases, different in the solution composition, were simulated. In Case 1, Phases A and C (water and gas) were mixed at 75% (molar) of water and 25% of gas, while in Case 2 the composition was at 80% and 20%, respectively. Both compositions lie on the binodal part of the Helmholtz energy surface (Stanley, 1971) meaning that the mixture is metastable. That is the mixture gradually decomposes to the stable phases under the influence and around of finite disturbances such as presence of surfaces wet by one of the phases. This contrasts with the spinodal, absolutely unstable mixtures, that undergo phase transitions almost instantly and involving the entire volume of the fluid. However, to our understanding, distinguishing between these two processes is uncommon in the flotation science.

Numerical simulation results for Case 1 are shown in Fig. 3.3.2. The results are presented in a form of separate movie frames captured at different consecutive moments in time 0.27 s, 0.375 s, 0.525 s, and 1.05 s. At 0.27 s, the droplets came noticeably downwards since their density is bigger than the density of the liquid-gas solution. Also, being hydrophobic, the droplets have attained a uniform layer of gas over their surface. When the gas layer grows above the equilibrium thickness, it sprouts the bubbles that are visible at 0.375 s; at this stage, the accumulated gas still does not support the droplets' weight and they continue settling down. Further on, at 0.525 s, the bubbles grew and drawn in most of the gas layer since the acting interfacial tensions do not support gas layers of macroscopic thickness (contact angle is non-zero); now the droplets are floating up. At 1.05 s, the bubbles are observed already coalesced at the top of their "host" droplets and the agglomerates are rising up.

In Case 2 (Fig. 3.3.3), the initial solution, although unstable too (metastable), is yet more stable than in Case 1. As the result, the process of flotation evolves much slower and passes several interesting stages. The simulation movie frames were captured at consecutive moments in time 0.459 s, 0.645 s, 0.945 s, 1.16 s, 1.22 s, 1.59 s, 1.97 s, and 2.7 s. At 0.459 s, the droplets are settling down, with the lowest one having reached the floor of the model; at the same time, the layer of gas accumulating on the droplets' surface is still thin as compared to similar moment in time of Case 1. Eventually, at 0.645 s, the gas accumulates and bubbles appear. At 0.945 s, the bubbles are observed coalesced at the top of the respective droplets and everything is rising up. However, as observed at 1.16 s, due to occurred lateral shifts and movements, two of the droplets came in contact and have coalesced; the same did some of the bubbles. Further on, at 1.22 s, because of wild oscillations caused by coalescence of the relatively big fluid bodies, the remaining liquid

droplet has also come in contact with the new big liquid droplet, and now there is only one big liquid droplet supported by a big bubble. This support is too much for the bubble, and it drops the droplet as is seen at 1.22 s. The bubble quickly rises up to the top of the model, while the deserted droplet with only a small bubble atop starts journey downwards (the image at 1.59 s). At the moment the droplet reaches the floor (at 1.97 s), the bubble has grown considerably. Eventually, at 2.7 s, it is already big enough for the agglomerate to rise up again.

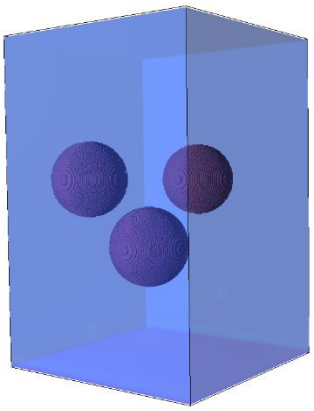


Fig. 3.3.1. Example 3. 3D view of the initial conditions. The ambient liquid with dissolved gas is shown in semitransparent blue, and the liquid droplets of Phase B are shown in red.

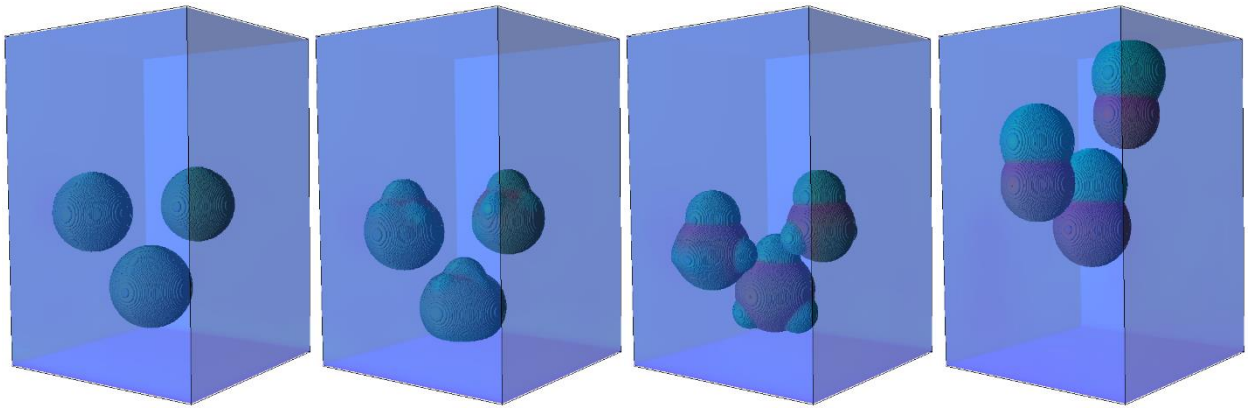


Fig. 3.3.2. Example 3, Case 1. 3D view of the distribution of phases at consecutive moments in time at 0.27 s, 0.375 s, 0.525 s, and 1.05 s (left to right). The ambient liquid with dissolved gas is shown in semitransparent blue, the appearing gas Phase C is shown in green, and the liquid droplets of Phase B are shown in red.

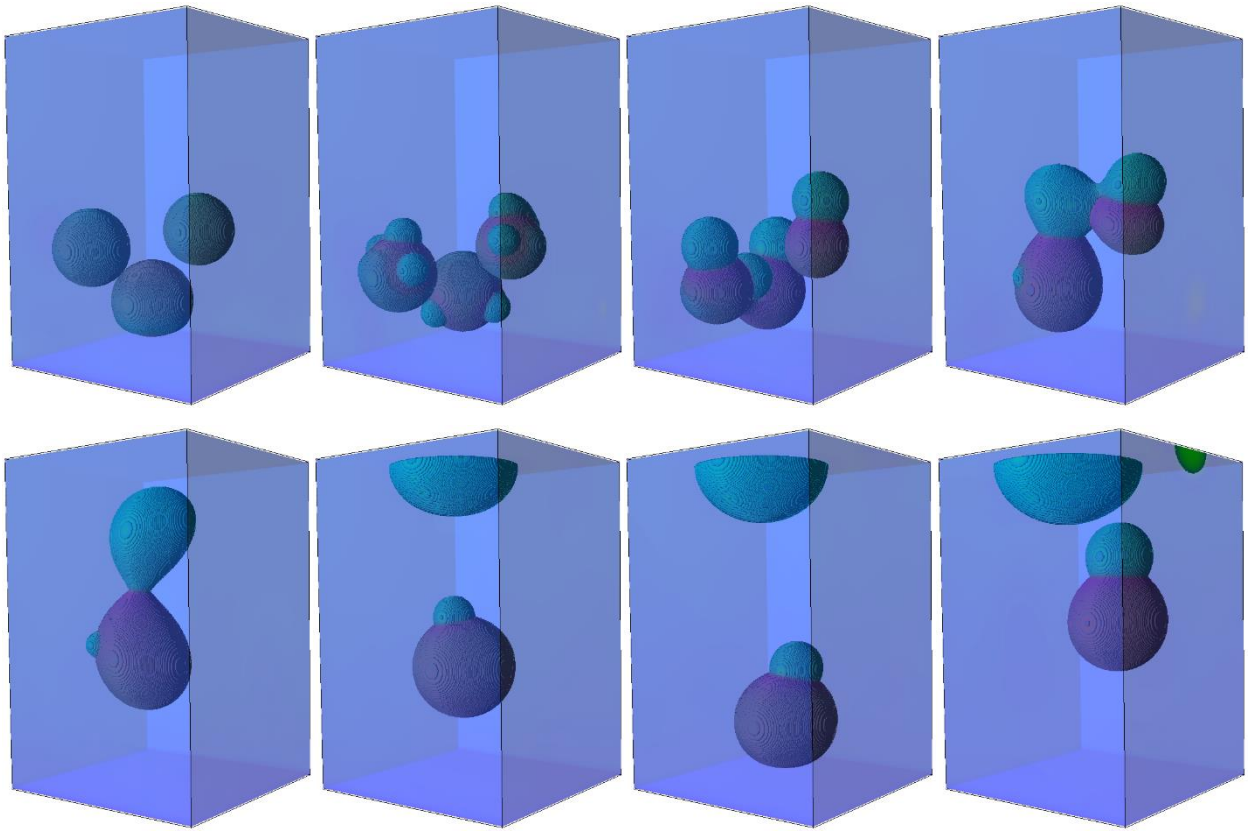


Fig. 3.3.3. Example 3, Case 2. 3D view of the distribution of phases at consecutive moments in time at 0.459 s, 0.645 s, 0.945 s, 1.16 s, 1.22 s, 1.59 s, 1.97 s, and 2.7 s (top row left to right, then bottom row left to right). The ambient liquid with dissolved gas is shown in semitransparent blue, the appearing gas Phase C is shown in green, and the liquid droplets of Phase B are shown in red.

4. Conclusions

In this paper, we demonstrated direct numerical simulation of the fundamental flotation mechanisms related to both interfacial energy balance and inertial phenomena. The simulations have been carried out by solving numerically the DFH equations.

Firstly, we showed simulation of fundamental mechanisms using simple statements involving just one gas bubble and one liquid droplet or solid particle. Such statements are convenient for detailed observation of individual aspects pertaining to the capturing and flotation processes. We demonstrated that depending on hydrodynamic regime the droplet or particle can be either successfully brought up or dropped by the rising bubble.

Secondly, we presented two simulation series with multiple gas bubbles and several liquid droplets or particles. The resulting flotation processes exhibited complex succession of events that we tried to describe.

Finally, we demonstrated modelling of DAF with several liquid droplets involved. The simulations have been carried out at different initial solution compositions corresponding to different gas saturations.

In this work, we do not claim that we have encompassed the complexity of the flotation mechanisms; we rather tried to demonstrate modelling possibilities. The detailed study of the processes we encountered in the modelling can be the subject of multiple specific papers. Also, many assumptions used in the present work, while convenient for demonstration, may not be best in terms of industrial use. Making the statements closer to the practical problems can be the focus of future work.

With use of relevant microfluidic simulations, it can be possible to develop population balance models related to specific conditions with account for particles wettability, interfacial tensions, viscosities, diffusion rates, flow regimes, and collective effects. This should also be the subject of future work.

ACKNOWLEDGEMENTS

We thank Schlumberger for permission to publish this work. We are grateful to Denis Klemin and Vladimir Khan for conducting internal review of the manuscript. We also thank our local colleague Mikhail Stukan for the gift of molecular dynamics simulation image incorporated within Fig. 1.

REFERENCES

R.T. Armstrong, N. Evseev, D. Koroteev, S. Berg, Modeling the velocity field during Haines jumps in porous media, Adv. Water Resour., **77**, 57–68 (2015)

R.T. Armstrong, S. Berg, O. Dinariev, N. Evseev, D. Klemin, D. Koroteev, and S. Safonov, Modeling of pore-scale two-phase phenomena using density functional hydrodynamics., Transp. Porous Med., **112**(3), 577 (2016).

D. Bonn, J. Eggers, J. Indekeu, J. Meunier, and E. Rolley, Wetting and spreading, Rev. Mod. Phys. **81**, 739 (2009).

R. Clift, J.R. Grace, and M.E. Weber, Bubbles, drops and particles (Academic press, New York, 1978).

Z. Dai, S. Dukhin, D. Fornasiero, and J. Ralston, The inertial hydrodynamic interaction of particles and rising bubbles with mobile surfaces, J. Colloid Interface Sci., **197**, 275–292 (1998).

A. Demianov, O. Dinariev, and N. Evseev, Density functional modeling in multiphase compositional hydrodynamics, Can. J. Chem. Eng., **89**, 206–226 (2011).

A.Yu. Demianov, O.Yu. Dinariev, and N.V. Evseev, Introduction to the density functional method in hydrodynamics (Fizmatlit, Moscow, 2014).

B.V. Derjaguin, Theory of stability of colloids and thin films (Consultants Bureau, New York, 1989).

O.Y. Dinariev, A hydrodynamic description of a multicomponent multiphase mixture in narrow pores and thin layers, J. Appl. Math. Mech. **59**(5), 745–752 (1995).

O.Y. Dinariev, thermal effects in the description of a multicomponent mixture using the density functional method, J. Appl. Math. Mech. **62**(3), 397–405 (1998).

O. Dinariev and N. Evseev, Multiphase flow modeling with density functional method, Computat. Geosci., **20**, 835 (2016).

O. Dinariev, N. Evseev, Modeling of nanoscale liquid mixture transport by density functional hydrodynamics, Phys. Rev. E **95**, 063307 (2017).

M.C. Fuerstenau, G. Jameson, and R.-H. Yoon (Ed.), Froth Flotation: A Century of Innovation (Society for Mining, Metallurgy, and Exploration, Inc., Littleton, Colorado, USA, 2007).

P. Hohenberg and W. Kohn, Inhomogeneous Electron Gas, Phys. Rev., 136, B864–B871 (1964).

E. Ivanov, N. Evseev, O. Dinariev, Rheological Effects in Two-Phase Microflow, Proceedings of the International Conference on Heat Transfer and Fluid Flow. Prague, Czech Republic, August 11-12, 2014.

P.T.L. Koh and M.P. Schwarz, CFD modelling of bubble–particle collision rates and efficiencies in a flotation cell, Minerals Engineering, **16**, 1055–1059 (2003)

P.T.L. Koh and M.P. Schwarz, CFD modelling of bubble–particle attachments in flotation cells, Minerals Engineering, **19**, 619–629 (2006).

W. Kohn, Nobel lecture: Electronic structure of matter—wave functions and density functional, Rev. Mod. Phys. **71**(5),1253–1266 (1999).

W. Kohn and L.J. Sham, Self-consistent equations including exchange and correlation effects, Phys. Rev., **140**, A1133–A1138 (1965).

V.G. Levich, Physicochemical hydrodynamics (Prentice-Hall, NJ, USA, 1962).

L. Li, H. Hao, Zh. Yuan, J. Liu, Molecular dynamics simulation of siderite-hematite-quartz flotation with sodium oleate, Applied Surface Science **419**, 557–563 (2017).

Marchisio, D. L. and Fox, R. O. Computational models for polydisperse particulate and multiphase systems (Cambridge University Press, Cambridge, 2013).

A.V. Nguyen, H.J. Schulze (Ed.), Colloidal Science of Flotation (Surfactant Science, Vol 118) (CRC Press, Boca Raton, Florida, USA, 2003).

L. Pan, S. Jung, and R.-H. Yoon, Effect of hydrophobicity on the stability of the wetting films of water formed on gold surfaces, J. Colloid Interface Sci., **361**, 321–330 (2011).

R.G. Parr and W. Yang, Density-Functional Theory of Atoms and Molecules (Oxford University Press, New York, 1989).

I. Prigogine, Introduction to thermodynamics of irreversible processes (Interscience Publ., New York, 1961).

B. Rai (Ed.), Molecular Modeling for the Design of Novel Performance Chemicals and Materials (CRC Press, Boca Raton, FL, USA, 2012)

J. Ralston, S.S. Dukhin, N.A. Mishchuk, Inertial hydrodynamic particle–bubble interaction in flotation, Int. J. Miner. Process., **56**, 207–256, (1999).

D. Ramkrishna, Population balances: Theory and applications to particulate systems in engineering (Academic press, San Diego, 2000)

J.S. Rowlinson, B. Widom, Molecular Theory of Capillarity (Clarendon Press, Oxford, 1982).

D.L. Russell, Practical Wastewater Treatment. (John Wiley & Sons, Hoboken, NJ, USA, 2006).

L.I. Sedov, Mechanics of continuous media. Vol.1. (World Scientific, New York, 1996).

H.E. Stanley, Introduction to Phase Transitions and Critical Phenomena (Oxford University Press, Oxford and New York, 1971)

H. Ström, M. Bondelind, S. Sasic, A novel hybrid scheme for making feasible nnumerical investigations of industrial three-phase flows with aggregation, Industrial & Engineering Chemistry Research, **52**, 10022–10027 (2013).

M. Su, W. Han, Z. Zhang, R. Li, Q. Li, W. Ma, Numerical simulation and analysis of gas-solid-liquid three-phase flow in mechanical flotation cell, Procedia Engineering **31**, 850 – 856 (2012).

C. Truesdell and W. Noll, The non-linear field theories of mechanics (Springer-Verlag, Berlin, 2004).

S.M. Walas, Phase equilibria in chemical engineering (Butterworth, Boston, 1985).

L.K. Wang, N.K. Shammas, W.A. Selke, and D.B.Aulenbach (Ed.), Handbook of environmental engineering, Vol. 12, Flotation technology (Humana Press, New York, 2010)

B.A. Wills and J.A. Finch, Wills' Mineral Processing Technology: An Introduction to the Practical Aspects of Ore Treatment and Mineral Recovery. 8th edition (Butterworth-Heinemann, Oxford, 2015).